Article | Received 22 November 2025; Revised 6 January 2026; Accepted 7 January 2026; Published 29 January 2026
https://doi.org/10.55092/am20260004

Transforming machining waste into functional SS316 foams through inert-atmosphere microwave sintering intended for crash boxes and improving crashworthiness of vehicles

Sanket Shinde[1,2], Siddharama Adi[2,3], Padmakumar Annasab Bajakke[4] and Vinayak Raghunath Malik[2,3,*]

[1] Department of Mechanical Engineering, D.Y. Patil College of Engineering and Technology, Kolhapur-416006, Maharashtra, India
[2] Visvesvaraya Technological University, Belagavi-590018, Karnataka, India
[3] Department of Mechanical Engineering, KLS Gogte Institute of Technology, Belagavi-590008, Karnataka, India
[4] Department of Mechatronics Engineering, Sharad Institute of Technology College of Engineering, Yadrav-Ichalkaranji-416121, Maharashtra, India

* Correspondence author; E-mail: vrm@git.edu.

Highlights:

- Green microwave sintering is employed to produce SS316 foams from turning chips.
- Progressive chip bending and buckling enhanced compressive energy absorption.
- Microwave-sintered foams form interconnected porous network via chip interlocking.
- Carbamide decomposes < 600 °C during sintering, yielding tailored foam porosity.

Abstract: The rate of recycling and scrap recovery is poised to rise significantly in the near future, reflecting a strategic commitment to long-term environmental and sustainable manufacturing practices. Advancing circular economy goals in line with UN SDG-12 requires innovative strategies, such as reusing machining chips in to metal foams. Machining chips have increasingly become a preferred feedstock for solid-state reuse, offering a sustainable alternative to conventional remelting. The present research aims to develop a novel and sustainable manufacturing route for reusing Stainless Steel 316L turning chips in metallic foam fabrication. The process employed microwave sintering at 1050 °C and 1200 °C under an inert-argon atmosphere. Sintering in an inert environment offers the added advantage of minimizing oxidation and contamination while enabling a more efficient sintering cycle. Three types of foams were fabricated: pure chip foams, hybrid foams and space-holder foams, and subsequently characterized for macrostructure, microstructure and compressive behavior to evaluate their physical and mechanical properties. Foams sintered at 1200 °C exhibited a more stable plateau region with enhanced energy absorption, while their lower plateau stress facilitated easier deformation under compression, rendering them highly impact-resistant and suitable for crashworthiness applications.

Keywords: Stainless Steel 316 Foams; turning chips; inert atmosphere; microwave sintering

1. Introduction

The World Steel Association (2025) reported that global steel consumption in 2024 reached ~1,742 million tonnes, reflecting its extensive use across industries [1]. Globally 14.6% of steel is being wasted in the form of chips [2]. In 2024, the global steel scrap market was estimated at 543.2 MMT and is expected to expand to 727.1 MMT by 2030, reflecting a CAGR of 5% over the forecast period [3]. Currently, machining chips are recycled through remelting, with scrap metal processed in EAF alongside virgin-metals, fluxes and reducing agents to facilitate purification and alloying. Producing 1-ton of scrap-based iron typically consumes roughly 1.2 tons of iron ore, 0.7 tons of coal, 0.5 tons of limestone, and considerable energy [4]. Although machining chips recycling reduces reliance on primary ores, major drawbacks include ~20% of burnout/oxidation loss, increased labour and energy cost [5–7]. In ESR and VAR furnaces, consumable electrodes produced by vacuum induction melting in open-top molds are prone to severe cracking from oxidation and turbulence during top pouring. These biofilms (double oxide films), appearing as cracks in the cast electrode, are a major source of VAR ingot defects [8]. Recycling offers strong economic and environmental benefits, yielding up to 50% cost reduction [9] and ~642 kWh energy savings per ton [10]. Iron and steel production accounts for roughly 9% of global CO_2 emissions, including ~1% from remelting machining waste [1,2]. To mitigate the carbon footprint associated with steel usage across industries, steel engineers must advance sustainability initiatives aligned with the UN's SDG 12 [11]. Industrial sectors can advance this goal through material recycling, with steel foams emerging as a viable alternative to bulk steel.

By tailoring density through controlled porosity, metallic foams reduce material consumption with pore morphology adjustable via fabrication methods such as LM and PM. LM is employed for closed-cell foams and, to some extent, open and lotus-cell foams; however, foaming molten metals remains inherently challenging [12,13]. PM is favored for open-cell foams and partially for closed-cell types, where oxide particles formed from powder fracture govern foam stability [14]. This approach offers uniform pore morphology and ~95% material utilization [15], though precursor preparation increases cost. In PM, advancing beyond conventional sintering requires the adoption of MWS [16], which provides rapid and uniform volumetric heating, shorter cycles, lower processing temperatures and substantial energy savings. Unlike conventional surface-to-core heat transfer, microwave energy penetrates the bulk, refining microstructure and enhancing mechanical properties.

Initially explored in the 1950s, metal foam fabrication gained industrial traction in the 1990s when Shinko Wire Company, Japan, developed scalable methods for automotive and acoustic uses [17]. Banhart *et al.* optimized Al foam production via PM using Al alloy and TiH_2, identifying 1 wt % foaming agent as optimal [18]. Considering material loss and input costs, researchers have explored the use of machining chips for production of metal foams. This route predominantly yields closed-cell foams, typically fabricated using TiH_2 as the foaming agent. Table 1 provides a brief overview of the studies conducted on chip-based foams.

Compared to Al foams, studies on SS foams remain limited, and their deformation mechanisms are not fully characterized. Fabrication of open-cell foams from alloys such as 316L, 314, 430L, Fe–0.6P martensitic and FeCrAl steels showed closed pores and edge defects, though their effects on deformation were not reported [19]. Kaya *et al.* [19] investigated SS316L foams with inherent microporosity,

combining digital image correlation with *in situ* SEM loading. They demonstrated that closed pore distribution strongly influences plateau stress via cell-face stretching, while strut buckling and bending dominate cell collapse. Hu *et al.* [20] examined SS316L foams produced by powder metallurgy with urea space holders, showing that higher porosity reduces yield strength and plastic modulus but increases densification strain. Energy absorption per volume decreased with porosity at constant strain. Bekoz and Oktay [21] further reported steel foams fabricated with different carbamide particle shapes. Their compressive yield strengths deviated from Gibson–Ashby predictions at low relative densities, revealing that cell-face stretching contributes linearly, whereas edge bending contributes nonlinearly, to foam strength and stiffness.

In metal foam fabrication, stainless steel powders have been predominantly investigated using conventional powder metallurgy routes, while aluminum machining chips have been processed mainly through extrusion-based solid-state methods. In contrast, the present work establishes a novel and sustainable manufacturing route based on the solid-state reuse of SS316 turning chips for metallic foam production. For the first time, inert-atmosphere microwave sintering is employed to consolidate SS316 turning chips into metallic foams, enabling improved inter chip bonding and material integrity compared to ambient condition processing [22]. Furthermore, three architecturally distinct foam configurations *i.e.*, pure chip foams (PCF), hybrid foams (HF) and space holder foams (SHF) are fabricated and characterized through macro and microstructural analyses, compression testing and evaluation of physical properties within a single study. The combined implementation of inert argon microwave sintering and comparative architectural evaluation of SS316 chip-based foams constitutes the central novelty of this study.

Table 1. Summary of research investigations on chip-based foams.

Primary Chip Material	Foaming Agent/ Space Holder Material	Processing Route	Principal Findings	Reference
AA6063	TiH_2 in 0.5 to 3.0 mass% and Al_2O_3 in 3 to 5 vol %	Hot Extrusion (723 K) and Compressive Torsion	• Optimal TiH_2 range exists; additions above 3 mass% do not improve pore formation.	[23]
AA6063 and AA4032	TiH_2 in 1 mass% and Al_2O_3 in 5 vol %	CT	• Higher low-solidus content increases porosity but reduces pore size	[24]
AlMg4.5Mn and AlSi9Cu3	CaCO3 – 3 wt % and $CaMg(CO_3)_2$ – 5 wt %	Thixo-casting Process	• $CaMg(CO_3)_2$ foams gain stability from MgO formation.	[25]
Al-Si-Cu (A383 alloy)	TiH_2 – 1 mass%	FSBE	• Exhibited compression behavior similar to solid-precursor foams.	[26]
EN AW 2011	Table Salt, Himalayan Salt and Urea	PM	• Exhibited the improved compressive strength-to-density and energy absorption-to-density ratio.	[27]
A380	TiH_2 in 0.5 wt % to 1.5 wt %	Hot Extrusion (400 °C)	• Higher temperature and foaming agent raised pore inhomogeneity, while lower TiH_2 at high temperature improved energy absorption and YS.	[28]
A360, A380, AA6082, AW 6082 and AA 7075	TiH_2 and $CaCO_3$	-	• TiH_2 -based foams, irrespective of the matrix, showed uniform pores and reduced relative density.	[29]
Clad chips - AA1050 sheets with TiH_2 spread in between	TiH_2 – 2 mass%	Backward Extrusion	• EAF heating at 700 °C gave ~51% porosity in clad chips, *vs.* ~20% in as-received AA1050.	[30]

2. Materials and methods

In this study, three types of foams *i.e.* PCF, HF and SHF, were fabricated by compacting chips in a single-acting hydraulic press followed by MWS under an inert atmosphere (Figure 1). The foam sample measures 25 mm in diameter and ~38 mm in height. The primary raw material consists of machining chips generated from SS316 turning operation, appearing as curled, continuous with an average length of 50–60 mm and thickness below 1 mm.

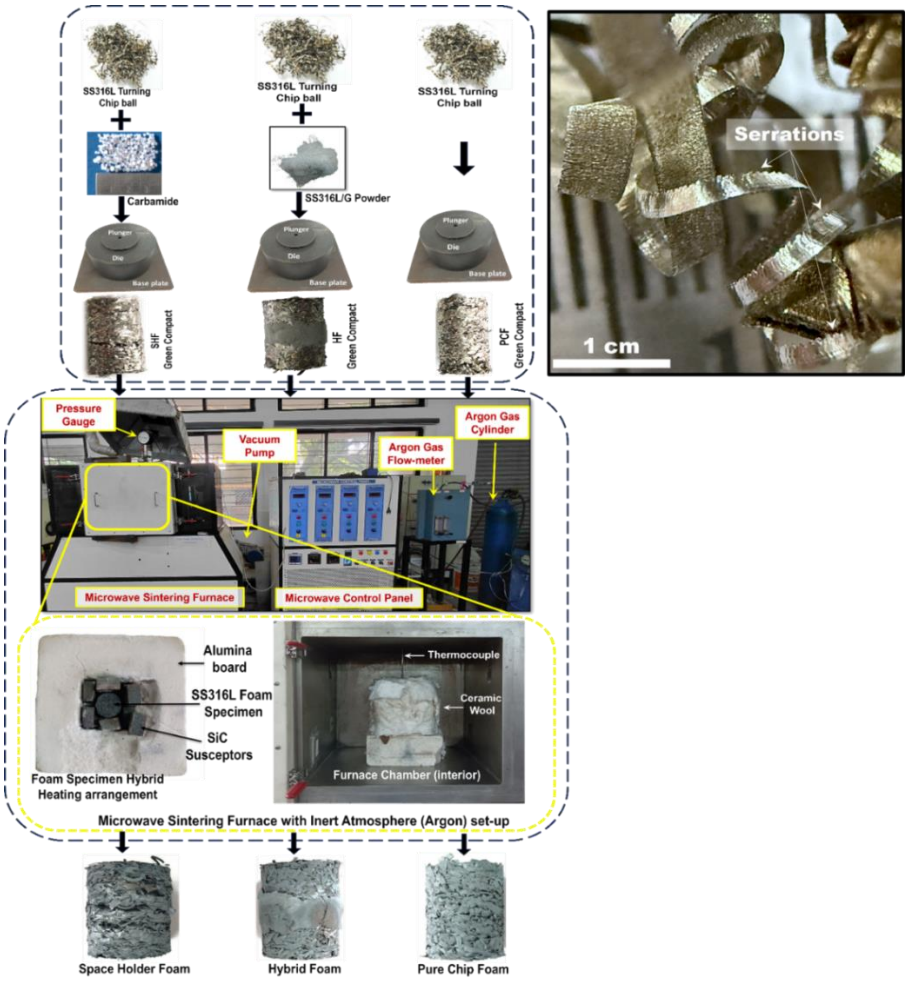

Figure 1. Process flow diagram: **(a)** Schematic representation of the fabrication route for SS316L foams derived from machining chips and **(b)** SS316 turning chips showing pronounced serrated morphology.

Owing to the severe plastic deformation imparted during machining, the chip macrostructure differs significantly from the bulk material. In ductile alloys such as SS316, intense shear within the primary shear zone gives rise to lamellar layers in the chip. This localized shear deformation typically induces true strains in the range of 0.5–1.5 for thin chips [31]. Consequently, elongated and highly strained micro-constituents are formed, aligned along the chip flow direction as a direct outcome of the turning process (Figure 1b).

For fabricating PCF, a total of 75 g of chips was compacted in 6 successive steps, with 12.5 g of chips added and sequentially compacted (1 MPa) until the final sample was obtained. The hybrid foams were fabricated using SS316 in two forms: chips and powder, with chemical composition shown in Table 2. Two foam designs were prepared: (i) 3 stacks with alternating 9 mm chip-powder-chip layers and (ii) 5 stacks with alternating 9 mm chip and 5 mm powder layers. To prepare the HF-powder layers,

100 g of SS316L powder with average particle size 63 µm was mixed with 5 wt % PVA binder was blended, placed in a die and compacted at 5 MPa. The PVA binder solution was prepared following the procedure reported in our previous study [22]. The compacted powder was then sliced to the required heights (9 mm and 5 mm) and manually inserted between the preformed chip compact-layers. The chips and powder compacts were surface-scraped, stacked alternately and manually compacted to ensure intimate interlayer contact. The SHF was fabricated using SS316 chips and near-spherical carbamide particles (1.5–3 mm) with smooth surfaces as the space holders. Initially, 50 g of SS316 chips were divided into five 10 g chip-balls, each mixed separately with 10 wt % (5 g), 15 wt % (7.5 g), and 20 wt % (10 g) carbamide particles. After adding each 10 g chip-ball to the die cavity, the specimen was lightly compacted at < 0.3 MPa and the surface scraped to preserve irregularity for improved interlayer bonding. This process was repeated for all five chip-balls (50 g SS316 chips), followed by final compaction at 1 MPa to obtain a uniform, cohesive green compact. Further, the compacted PCF, HF and SHF were microwave sintered (4 magnetron 1.4 kW each) in an inert argon atmosphere. Samples were sintered at 1050 °C and 1200 °C with a 7-minute soak. Due to metal reflectivity, a hybrid setup was used, wherein the foam was surrounded by SiC susceptors and insulated with an alumina board and glass wool (inset, Figure 1a). To prevent oxidation and scale formation observed in prior ambient atmosphere MWS [22], the chamber was evacuated to 10 mm Hg (> 96% air removed) and purged with argon at 2 LPM for 5-minute. Sintering proceeded under the same Ar flow. Corresponding time–temperature profiles are shown in Figure 2.

The fabricated foam samples were evaluated for physical and mechanical properties. Porosity, density and macro and microstructure were analyzed. Macrostructural images were captured at 10× using a METLAB trinocular stereo zoom microscope, while microstructural characterization employed a Dino-Lite optical microscope and a Vega3 TESCAN SEM at 5 kV to examine sintering necks and chip orientation. XRD was performed to assess phase composition and to evaluate the influence of the inert Ar atmosphere. Compression tests were conducted on a TUE-C-400 UTM (400 kN capacity, 0.04 kN least count) to obtain true stress–strain curves and determine mechanical parameters such as plateau stress, energy absorption, and densification strain.

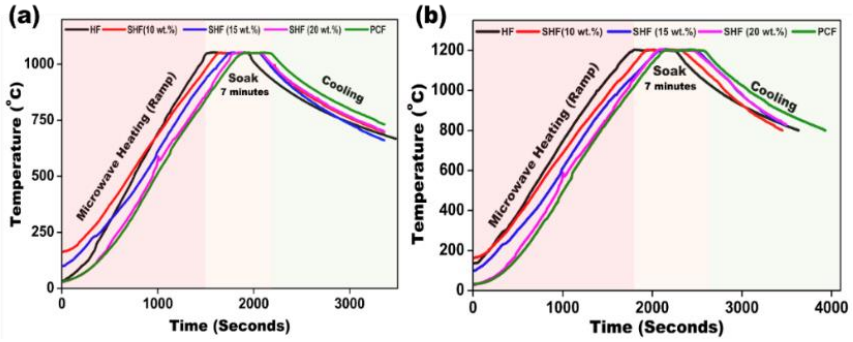

Figure 2. Microwave heating cycles at **(a)** 1050 °C and **(b)** 1200 °C.

Table 2. Chemical composition of SS316 [22] and SS316L/G powder.

Material	Cr%	Ni%	Mo%	Mn%	Si%	C%	P%	S%	Fe%
SS316	16–18	10–14	2–3	2	0.75	0.08	0.045	0.03	Balance
SS316L/G powder	16–18	10–14	2–3	2.00 Max	1.00 Max	0.03 Max	0.02 Max	0.02 Max	Balance

3. Results and discussion

3.1. Physical properties, macro and microstructure

Table 3 highlight the foam samples with designated codes, process parameters, physical and mechanical properties. Stereo microscopy and SEM analysis of cross-section (Figure 3) reveal critical architectural details of the PCF foam. The foam exhibits a network of interconnected macropores generated by the random orientation of turning chips. Cross-sectional image reveals distinct stratification, where sequentially deposited chip clusters form elongated lamellae, separated by interconnected voids that create a continuous pore network across the material (Figure 3a). During pre-compaction, the chip inherent geometry promotes mechanical interlocking, forming a physically entangled 3D metallic skeleton. Chips display local waviness and curvature. The PCF develops into layered structure (Figure 3b), with the spiral chips spontaneously nesting within one another under a pressing load. Irregular contact points between chips establish a non-periodic yet mechanically stable framework, where load transfer occurs through point contacts and frictional resistance. Porosity within the structure is heterogeneous, with flattened pores arising from uniaxial pressing. Localized densification zones coexist with highly porous regions (flexural zones) (Figure 3c), leading to non-uniform morphology. This anisotropy and heterogeneity influence deformation behavior under compressive loading, making the entangled chip framework central to foam's energy absorption.

Table 3. Summary of process parameters, resultant physical and mechanical properties of foams compacted at 1 MPa and microwave-sintered with a 7-minute soak.

Specimen Name	Microwave Sintering Temperature (°C)	Final True Stress (σ_{fi}) (MPa)	Final True Strain (ε_{fi})	Plateau Stress (σ_{Pl}) (MPa)	Energy Absorption (EA) (MJ/m^3)	Specific Energy Absorption (J/g)	Porosity (%)	Density (ρ_f) (g/cm^3)
PCF-A	1050	274.435	0.959	20.133	112.936	26.93	51.93	3.80
PCF-B	1200	300.46	0.86	18.41	115.92	28.45	54.60	3.58
HF-A (2C & 1P)	1050	407.3	0.56	30.38	74.53	15.55	36.13	5.0
HF-B (3C and 2P)	1050	344.02	0.73	29.75	132.602	24.61	37.61	4.93
HF-C (2C and 1P)	1200	462.2	0.43	35.15	86.698	15.96	30.23	5.51
HF-D (3C and 2P)	1200	353.17	0.699	31.30	131.398	23.81	35.4	5.1
SHF-A (10% Carbamide)	1050	402.99	0.45	17.01	59.486	17.21	56.63	3.39
SHF-B (15% Carbamide)	1050	333.67	0.759	16.0	84.6795	25.80	58.52	3.26
SHF-C (20% Carbamide)	1050	276.41	0.953	15.13	59.2119	18.89	60.41	3.14
SHF-D (10% Carbamide)	1200	368.46	0.659	18.64	80.1577	21.78	54.25	3.61
SHF-E (15% Carbamide)	1200	213.33	1.194	18.10	96.922	27.069	54.66	3.54
SHF-F (20% Carbamide)	1200	279.63	0.940	15.71	46.5584	14.0934	59.30	3.22

Microwave Sintering Behaviour: The SS316 alloy begins to exhibit strong microwave absorption above ~200–300 °C (Regime II, volumetric joule heating starts) and maintains this behavior up to ~970–1140 °C, beyond which heating is predominantly governed by the susceptors [32]. Equation (1) was used to analyse

densification kinetics, with the grain growth exponent 'n' indicating the diffusion mechanism. The 'n' values of 2.186 (1100 °C) and 2.298 (1200 °C) in sintered samples indicate mixed type mechanism *i.e.*, surface diffusion (Figure 4c) with grain boundary retardation [32]. At these lower temperatures, surface-related defects and oxide films enhance microwave coupling, thereby accelerating surface diffusion [32]. Microwave heating has lower activation energies compared to traditional heating. These lower activation energies indicate that self-diffusion facilitate particle necking at contact points [32]. Turning chips are plastically deformed - curled, elongated, thin, with dense network of dislocations and internal strain. This high defect density lowers the activation barrier for diffusion-controlled processes (surface diffusion). The reduced activation barrier facilitates rapid necking and inter-chip bonding (once the solidus region ~1050–1200 °C is reached) [33] under microwave-hybrid heating, despite the predominantly susceptor-controlled heating profile, thereby enabling densification within short soak times. Thus, in PCF processed under microwave hybrid sintering in an Ar atmosphere with 7 minutes soak, initial densification is governed by solid-state surface diffusion as observed in Figure 3d. This mechanism facilitates the development of metallurgical necks that reinforce the mechanically interlocked chip framework while preserving its architecture. Nevertheless, not all regions achieve full consolidation, leaving portions of the structure with loosely bonded chips and visible interstitial voids. Figure 4a,b represent the porosity and density of the specimens. In PCF-A resulted in 51.93% porosity and 3.8 g/cm^3 density. While sample B accounted for a higher porosity of 54.6% and a lower density of 3.58 g/cm^3.

$$G_n = kt^n \exp\left(-\frac{Q_g}{RT}\right) \quad (1)$$

Where, Gn refers to the mean grain size (µm), n is the grain growth exponent, t denotes the isothermal holding time (min), Qg represents the activation energy for grain growth (J mol-1), k is the sintering-rate constant, R is universal-gas constant (8.315 J mol-1K-1) and T sintering temperature (K).

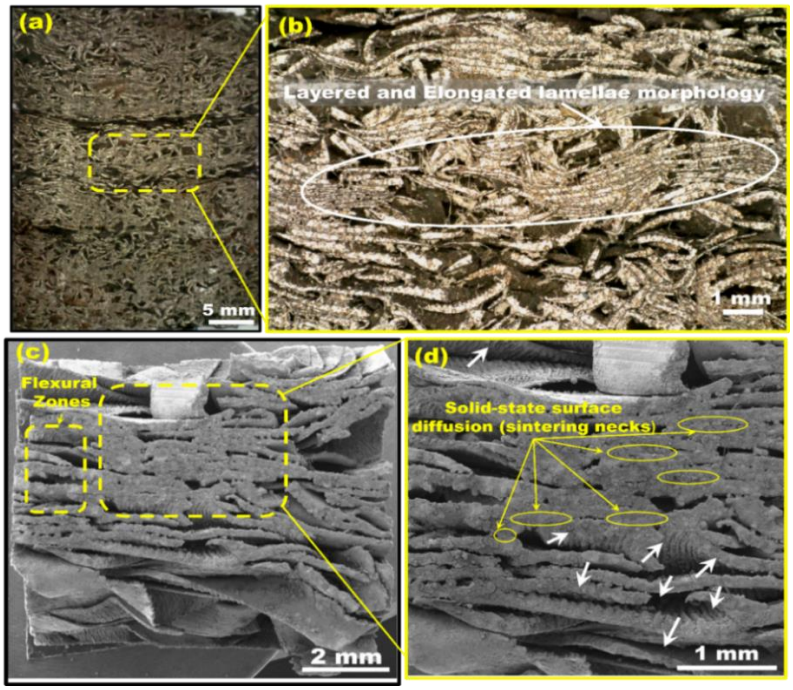

Figure 3. Macrostructures from Stereo and Scanning Electron Microscopes: **(a)** PCF CS macrograph, **(b)** Inset highlighting the spatial arrangement of SS316 chips, **(c)** SEM micrograph illustrating pore morphology in the sectioned PCF, with **(d)** inset emphasizing surface diffusion.

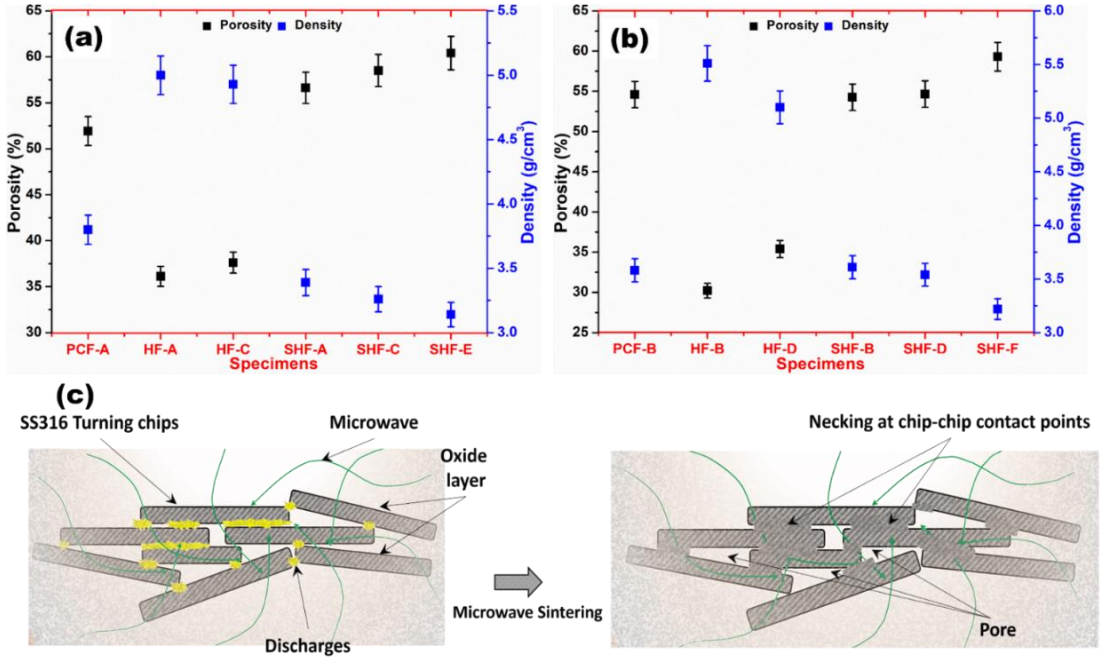

Figure 4. Porosity and density of foam specimens sintered at **(a)** 1050 °C and **(b)** 1200 °C, respectively; **(c)** Schematic illustration of the initial-stage surface diffusion mechanism between adjacent chips.

Figure 5a show a distinctly stratified three-layered HF with two porous SS316 chip outer layers and a denser SS316L powder core at center. The macro and microstructural analysis of the outer-chip-layers are characterized by primary inter-chip voids (Figure 5 b,c). The outer chip layers display a coarse and irregular pore morphology with interconnected voids, arising from the interstitial spaces between randomly packed turning chips, similar to those observed in PCF. In contrast, the central powder layer is more uniform and less porous, consisting of sintered SS316L particles forming a continuous solid phase with finer, evenly distributed porosity than the chip layers (Figure 5d). As observed in PCF, microwave sintering in chip regions promoted metallurgical bonding, forming distinct sintering necks at chip junctions (Figure 5c). The central powder layer showed greater material transport under microwaves, where surface diffusion (750–900 °C) [34] formed necks, yielding higher density and lower porosity than the chip layers. In the HF-A exhibited a porosity of 36.13% and density of 5.0 g/cm^3. In contrast, HF-B achieved the porosity of 37.61% with the density recorded at 4.93 g/cm^3. Figure 6c shows metallurgical bonding between deformed chips and powder particles through continuous sintering necks, indicating solid-state diffusion. However, these interfaces are also susceptible to differential densification during sintering. The powder layer, exhibiting increased surface area-to-volume ratio and greater packing density, generally exhibits a higher driving force for shrinkage and densification than the more stable, coarser chip layers. This difference in shrinkage rates can induce residual stresses at the interface, potentially manifesting as micro-cracks or increased interfacial porosity.

At the macroscale, the cross-sectional Figure 6 of SHF shows a network of interlinked pores of varying sizes and shapes distributed throughout the metallic matrix. This porous architecture is a result of two phenomena: (i) Inherent empty spaces between the irregularly shaped turning chips and (ii) Thermal decomposition and complete removal of the carbamide space-holder particles during the microwave heating cycle. Two distinct types of porosity can be identified. Inter-chip voids, these are

smaller, highly irregular pores, with dimensions often less than 300-500 µm (Figure 6b). Their shape is dictated by the geometry of the gaps between adjacent chips. Carbamide-induced pores as shown in Figure 6a, these are larger pores intentionally created by the decomposition of the carbamide particles with dimensions ranging from 1–2 mm. Similar to PCF, at the interfaces between adjacent chips, distinct sintering necks emerge (Figure 6c,d), formed through solid-state diffusion at sintering temperatures of 1050 °C and 1200 °C. The 7-minute soak ensures two things: first, all gaseous byproducts from the carbamide are completely purged from the system and second, sufficient time is provided for the formation of metallurgical sintering necks between the SS316 chips. Carbamide (urea, $CO(NH_2)_2$) does not decompose in a single step. Its thermal decomposition proceeds as shown in Equation (2). Carbamide melts at ~133–135 °C, enabling ionic rearrangement. Above its melting point, molten carbamide undergoes intramolecular rearrangement, yielding ammonium cyanate ($NH_4^+NCO^-$). Ammonium cyanate decomposes into NH_3 and cyanic acid (HNCO) gases. As the temperature continues to rise towards the sintering temperature, all intermediate organic compounds (biuret, triuret, cyanuric acid) fully decompose into volatile gases, primarily NH_3 and CO_2 [35,36].

$$H_2N\text{-}CO\text{-}NH_2\ (m) + \text{heat} \rightarrow NH_4^+NCO^-\ (m) \rightarrow NH_3\ (g) + HNCO\ (g) \quad (2)$$

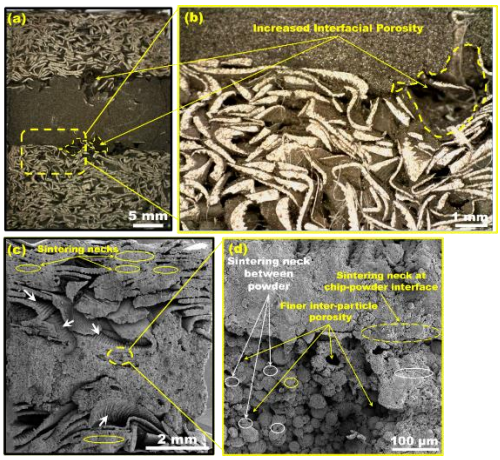

Figure 5. Macrostructures from Stereo and Scanning Electron Microscopes: **(a)** CS view of the HF illustrating variations in porosity and density across the thickness, with **(b)** inset highlighting porosity at the chip–powder interface; **(c)** SEM micrograph depicting inter-chip voids and developed sintering necks, with **(d)** inset showing neck formation at both chip–powder interfaces and inter-particle contacts.

Crucially, the entire decomposition process is completed at temperatures well below 600 °C. This temporal separation is vital as the space-holder is completely removed, leaving a pore network in its place, before surface diffusion of the chip matrix occurs. The SHF-A (56.63% and 3.39 g/cm^3), sample-B (58.52% and 3.26 g/cm^3) and sample-C (60.41% and 3.14 g/cm^3) witnessed the combination of maximum porosity with minimum density. Foams sintered at 1050°C exhibited higher porosity and lower density, as the lower temperature limited particle bonding and preserved open pore structures. In contrast, higher sintering temperatures produced denser materials with finer pores due to enhanced particle fusion. Overall, irrespective of sintering temperatures the foams with high porosity and low density are in the order of HF < PCF < SHF. The porosity of foams is calculated using the Equation (3)

$$P = \left(1 - \frac{\rho_f}{\rho_m}\right) * 100\% \quad (3)$$

Where ρ_f is the density of the foam and ρ_m is the theoretical density of SS-316 metal (≈ 8 g/cm^3). For SHF-C, the calculated porosity is 60.75% and for HF-C, it is 31.12%.

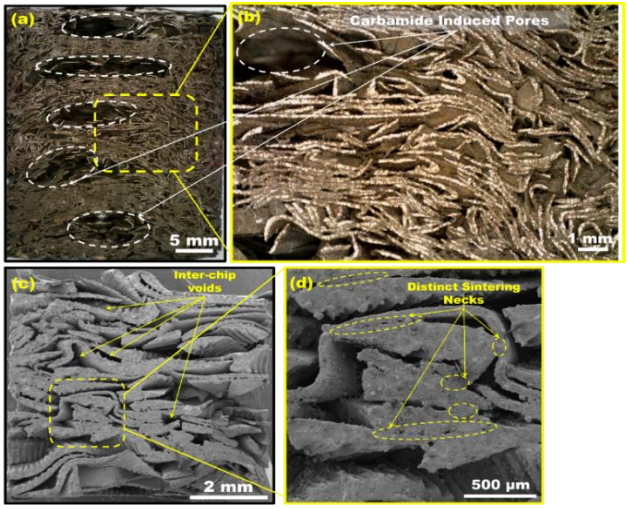

Figure 6. Macrostructures from Stereo and Scanning Electron Microscopes: **(a)** CS macrograph illustrating carbamide-induced porosity with **(b)** inset highlighting entangled metallic swarf; **(c)** SEM micrograph showing stratified chip lamellae with inter-chip voids, and **(d)** inset depicting sintering necks developed.

3.2. Compression response and deformation characteristics

The compressive stress–strain responses of the foam specimens are presented in Figure 7a,b. The plateau stress can be validated by the Gibson-Ashby model for open cell foams as given by Equation (4).

$$\sigma_p = \sigma_s \, C \left(\frac{\rho_f}{\rho_m}\right)^{3/2} \quad (4)$$

Where σ_p is foam's plateau stress and σ_s is the YS of solid SS-316 (≈ 205 MPa), C (≈ 0.3) is empirical constants for metal foams. Substituting the values for HF-A,

$$\sigma_p = 205 * 0.3 * (5/8)^{3/2} = 30.38 \text{ MPa}$$

For HF-A, the cross-validated plateau stress is 30.38 MPa which is almost near the experimental value of 30.66 MPa. The final strain (ε_{fi}) serves as an indicator of foam ductility and has been found to increase with porosity. This behavior arises from:

$$\varepsilon_f \propto \left(\frac{1}{\varepsilon_f}\right)^m \quad (5)$$

Here, m represents an empirical exponent. The experimental observations align with the predictive model, highlighting the role of pore distribution and interconnectivity [35]. Energy absorption (EA) properties of the foam structures were obtained by integrating the area under the compressive true stress–strain curves, as expressed in Equation (6). where σ denotes final stress and ε denotes final strain [37]

$$EA = \int_0^{\varepsilon_{fi}} \sigma d\varepsilon \quad (6)$$

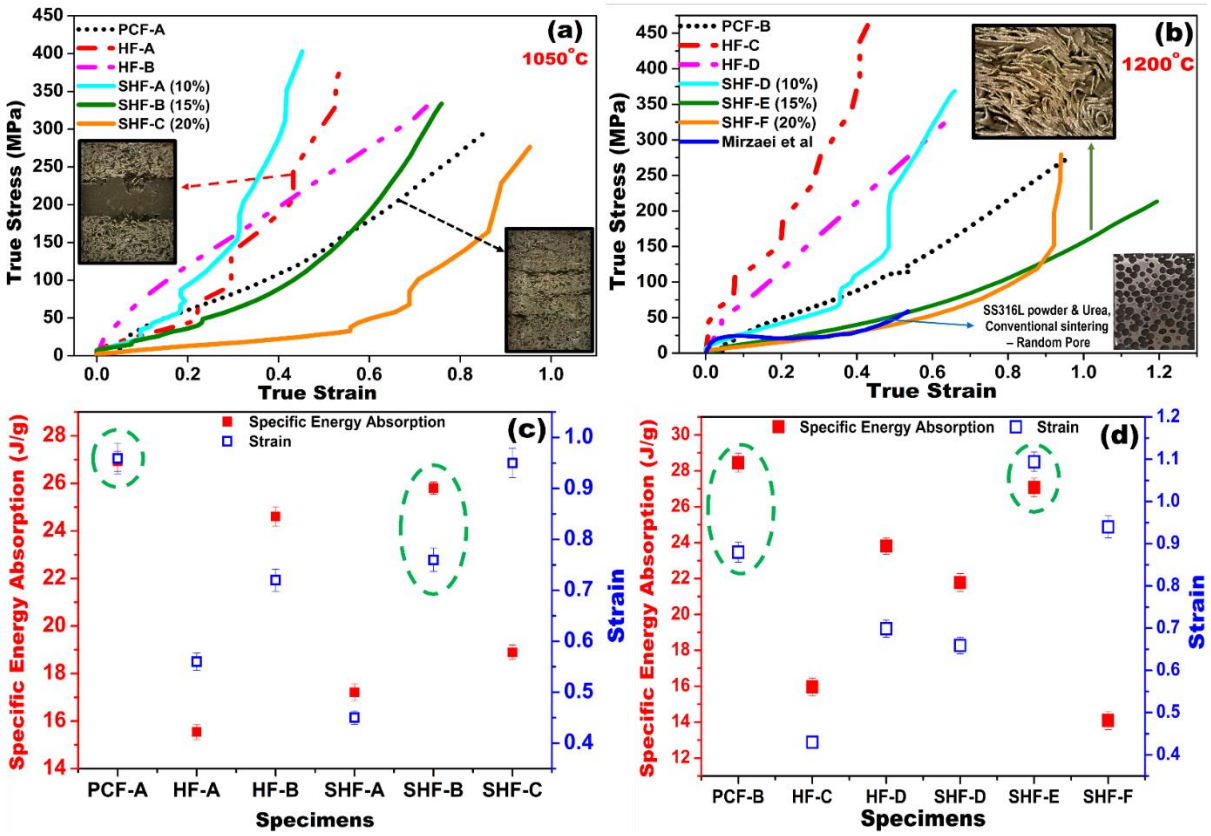

Figure 7. True stress and True strain of foam samples sintered at **(a)** 1050 °C and **(b)** 1200 °C. SEA (J/g), SEA and final strain of foam samples sintered at **(c)** 1050 °C and **(d)** 1200 °C.

A macro-level examination of the post-compression PCF (Figure 8a) reveals non-uniform densification, indicating progression beyond the elastic limit into plastic collapse. The notable feature is the formation of distinct collapse bands, representing regions of high strain where the material has been severely crushed. X-ray Computed Tomography studies confirm that compression reduces mean pore size and narrows pore distribution in metal foams [38]. The present image supports this, showing that large inter-chip voids are nearly closed in certain regions, transforming the foam into a near-solid mass. Remnant pores persist only in less severely compressed areas, appearing as small, irregular and tortuous voids shaped by the contorted chip surfaces. As the compression stress exceeds the elastic limit of the weakest members of the chip network, localized plastic deformation begins. This typically initiates at points of high-stress concentration, such as the sharpest bends in the chips or the thinnest sintering necks. The deformation quickly transitions to plastic bending and buckling of the chip walls. Larger pores with thin chip walls act as weak zones, while smaller pores with thicker walls provide stronger regions. Maximum pore collapse occurred in these weak zones (as shown in Figure 3), where large pores with thin chip walls existed prior to loading. Collapse begins in larger cells, while others linked it to pore shape; 3D studies by Kader *et al.* [39] identified cell-wall thickness as the key factor in permanent deformation. Pore collapse under uniaxial compression is noteworthy as it proceeds through an autocatalytic mechanism [39]. Deformation begins in a region of weak chip walls, after which the load is transferred to adjacent walls, causing sequential collapse of progressively weaker regions. This bending is not simultaneous across the specimen; rather, it nucleates in localized regions, forming collapse bands. These bands then propagate as neighbouring chip walls bend, buckle and flatten in

succession. The final stage, as depicted in the Figure 8b, occurs when opposing chip walls within the collapsed structure come into contact. Bending and buckling thus serve as the principal energy-absorption mechanisms during the plateau phase, where large strains (up-to 1) are accommodated at nearly constant stress. Compression tests (Figure 7) shows that the 1200 °C sintered sample (PCF-B) has lower plateau stress but slightly higher SEA compared to the 1050 °C sample (PCF-A). Plateau stress drops from 20.13 to 18.41 MPa (~8.5%) due to reduced relative density at 1200 °C. While higher temperature improves local chip contacts through enhanced sintering, it also promotes pore coarsening, leading to thinner load-bearing walls and thus lower density, consistent with Gibson–Ashby scaling. Despite this, volumetric energy absorption rises from 112.94 to 115.92 MJ/m³ and density decreases from 3.80 to 3.58 g/cm³, producing a ~6% increase in SEA. The mechanism is attributed to diffusion at 1200 °C, which strengthens chip-to-chip bonds but weakens inter-chip bridges, shifting the foam toward a more bending-dominated structure with slightly reduced plateau stress.

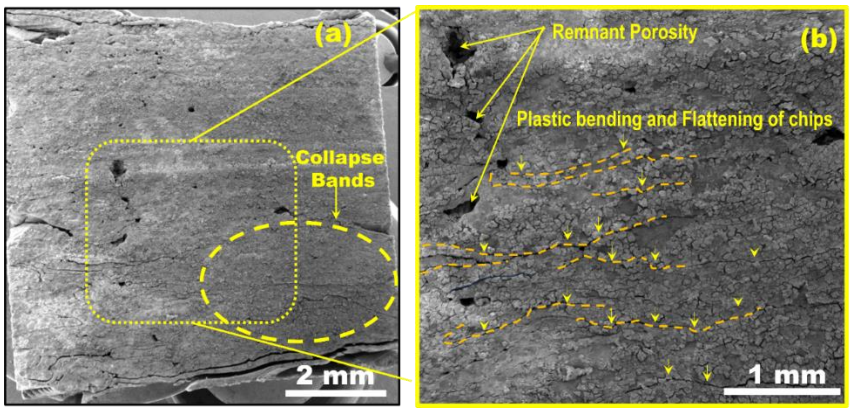

Figure 8. SEM images of **(a)** Post-compression PCF showing collapse bands; **(b)** inset illustrates chip bending, flattening and the presence of residual pores.

At the macrostructural scale, the compressed HF (Figure 9a) exhibits a complex and heterogeneous deformation pattern due to its layered architecture. The powder layer, with increasing load, it undergoes particle rearrangement and localized densification, although loosely bonded regions remain, indicating residual pore spaces that contribute to foam-like behavior. The mechanical response of HF diverges markedly from PCF, particularly in plateau stress and strain. In HF-C sample, sintered at 1200 °C achieved a plateau stress of 35.15 MPa with a final strain of 0.43, whereas the 1050 °C variant (HF-A) reached 30.38 MPa but extended strain to 0.56. A similar trend was observed in the HF-D sample (1200 °C) exhibiting 31.3 MPa and 0.69 strain, while its 1050 °C counterpart (HF-B) recorded 29.75 MPa and 0.73. These results demonstrate that higher sintering temperature enhances diffusion, producing stronger interparticle necks and raising plateau stresses, while simultaneously accelerating densification and reducing the deformation window. Since plateau stress in metallic foams scales with relative density (ρ_f/ρ_s) and bond strength, the increased densities of HF (5.0–5.5 g·cm^{-3}) relative to PCF and SHF, along with the layered configuration, both elevate stiffness and restrict pore-collapse propagation, thereby curtailing the extent of progressive deformation before densification.

Further, during MWS, the powder region densifies at a different rate than the chip layers because of its higher surface area. This differential densification creates a strain mismatch in the mechanical response between the powder and chip layers when subjected to compressive loading. The powder layer may become denser and stiffer in specific regions compared to the chip layers. As a result, the powder

layer can act as a constraint on the overall strain propagation within the foam. Instead of the strain distributing uniformly across the entire structure, it may localize preferentially in weaker areas or at the interfaces between the powder & chip layers. Therefore, leading to reduced final strain (0.4 to 0.7). The non-uniform density seen in the post compression (Figure 9a,b) is evidence of this localized collapse.

The SEM micrograph (Figure 10) of the SHF after the compression test depicts a mosaic-like, dense banded pattern, evidence of large-scale chip reorganization and macroscopic densification. Residual porosity appears as small, mostly isolated dark regions within the chip matrix (Figure 10b). The ductility of SS enabled chip walls to deform (bend and buckle) without catastrophic failure, driving adjacent chips into close contact and densifying the SHF. At the interfaces, the interaction between chips appears to involve a combination of mechanical interlocking and frictional sliding. A distinct, localized crush band has formed, oriented at an angle to the loading axis. This feature is consistent with the formation of a shear band as shown in Figure 10a, which is a common deformation mechanism in metallic foams under compression [40,41]. This band represents a zone localized collapse where the structure has been compacted to a much higher density compared to the adjacent regions. The areas outside this crush band, while compressed, retain a more open and porous structure. Increasing space-holder content reduces foam density and, as per Gibson–Ashby scaling, lowers plateau stress. The 15% space-holder content achieve an optimal trade-off as shown in Figure 7c,d. Below this, the foam may be too dense; above this (at 20%), the higher porosity may begin to compromise the plateau stress (σ_{pl}) and overall structural integrity, as seen in the drop in SEA from Foam-E (15%) to Foam-F (20%). Sintering temperature exerts an independent control. A 150°C rise accelerates diffusion, thickens necks and raises σ_{pl}, but simultaneously depletes compressible porosity.

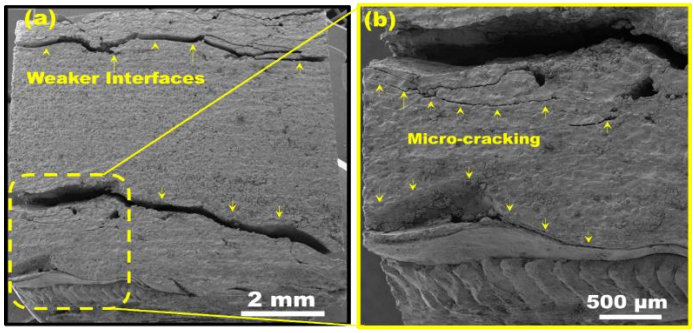

Figure 9. SEM images of **(a)** Post-compression HF illustrating weakened interfacial regions; inset **(b)** magnified view highlighting microcrack formation within the powder-rich zones.

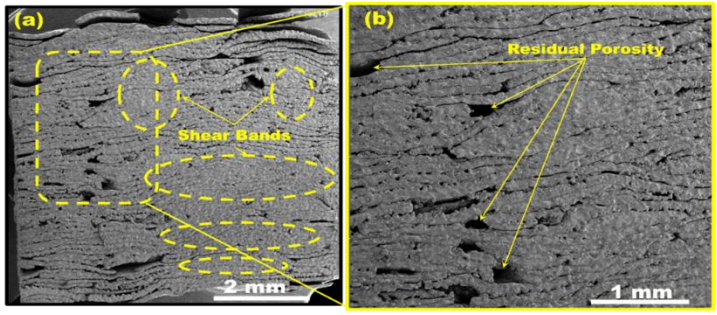

Figure 10. SEM images of **(a)** SHF Post-compression micrograph showing chip deformation through bending and buckling accompanied by localized densification (shear bands); inset **(b)** highlights residual porosity retained after compression.

The SS316L turning chip foams developed in this study offer several distinct advantages. The process utilizes machining waste enabling low cost and sustainable manufacturing, low pre-compaction pressure, solid-state route (avoids remelting losses), inert-microwave sintering with short cycle time, energy efficient and volumetric heating. The chip-based architecture enables stable deformation and no brittle collapse. The deformation is predictable, progressive and repeatable. Although the proposed approach offers several advantages, it also presents inherent limitations that requires critical discussion. Owing to the inherent heterogeneity in chip size and geometry, the resulting foams may exhibit some degree of property scatter and scaling the process for large components is a challenge. An additional limitation intrinsic to the reuse of machining chips is the presence of surface related contaminations introduced during the cutting process. Stainless steel turning chips typically exhibit surface oxidation, arising from high local temperatures combined with exposure to air and severe plastic deformation during machining process [42]. In addition, machining chips often retain residual moisture and organic contaminants originating from cutting fluids. These residues can decompose during heating, leading to localized gas evolution which may adversely affect densification uniformity and mechanical repeatability. The inert-atmosphere microwave sintering mitigates further oxidation but it does not fully eliminate the influence of pre-existing surface oxides and contaminants inherent to machining waste.

3.3. Application: automotive crash-box (energy-absorbing member)

A crash box is a thin metal structure placed between the vehicle bumper and the main body. Its purpose is not to remain rigid or strong during a collision. Instead, it is designed to deform in a controlled manner so that it can absorb the impact energy and reduce the force transmitted to the passengers [43]. By slowing down the vehicle gradually rather than abruptly, the crash box helps in improving passenger safety. The SS316L turning chip-based foams developed in this work demonstrate a new class of crash energy absorbers for electric/entry level lightweight vehicles. Unlike conventional powder based metallic foams that rely on brittle cell-wall collapse, the present foams dissipate energy through progressive chip bending through sintered necks, flattening and buckling particularly around large pores and inter-chip voids. When configured as a PCF, HF, SHF layered architecture within a crash box as depicted in Figure 11, the structure enables sequential deformation, reduced peak loads and exceptionally high specific energy absorption (up to ~27 J/g), making it ideally suited for lightweight/electric vehicle crashworthiness applications where battery safety and mass efficiency are critical. PCF already achieves SEA of 22–24 J/g, which is ~1.5 times higher than most powder-based SS foams reported in literature. During compression, the deformation is mainly bending dominated rather than sudden crushing. This behaviour makes PCF suitable for longer crash boxes with thin walls, typically in the range of 3 to 4 mm and for square or rectangular cross-sections. SHF achieves the highest SEA (27 J/g), not by increasing strength, but by delaying the onset of densification, which is enabled by its enhanced porosity, relatively low stiffness and extended densification strain regime. These characteristics make SHF particularly suitable for the front portion of crash boxes and for long, thin-walled tubular structures. The porous nature of SHF helps in reducing the initial peak force and allows the collapse to begin smoothly, which is desirable for improving crash safety. Studies such as those reported by Jiga *et al.* clearly show that crash box performance depends on a combination of factors. The geometry of the crash box mainly controls the folding pattern, while the foam density governs how strongly the structure resists deformation.

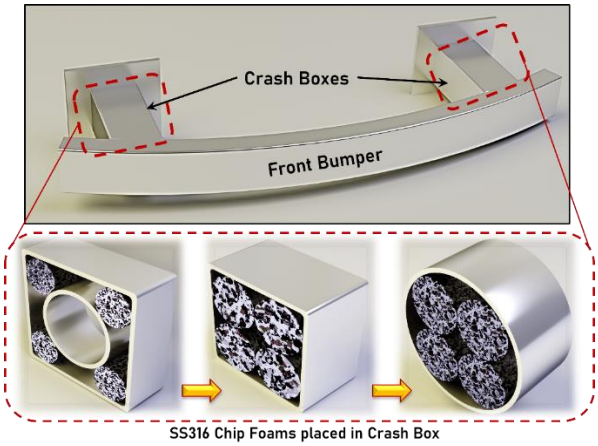

Figure 11. Conceptual integration of SS316 PCF, HF and SHF foams within automotive crash box geometries.

3.4. XRD Analysis

Foam samples with superior physical and mechanical properties were selected for XRD analysis, and the identified phases are shown in Figure 12a–d. Our previous study showed that MWS in ambient air promotes oxide formation [22]. To mitigate this, MWS was performed under an inert Ar atmosphere; however, oxide and nitride phases were still detected. The black soot-like deposition confirmed Magnetite (Fe_3O_4) phase. The secondary phase formation was consistently observed, including various iron oxides (Fe_2O_3, $Fe_{2.932}O_4$), chromium (II) oxide (CrO), and both iron (FeN_x) and chromium nitrides (Cr_2N). Oxides, such as Fe_2O_3 being a poor microwave absorber, although thin, introduce diffusion barriers, slowing down the neck formation [44]. Conversely, the formation of nitrides (FeN_x, Cr_2N) suggests beneficial interstitial strengthening and potentially enhanced load-bearing capabilities within the neck regions [45]. These microstructural differences likely influence sintering neck strength and, consequently, the foam's structural resilience.

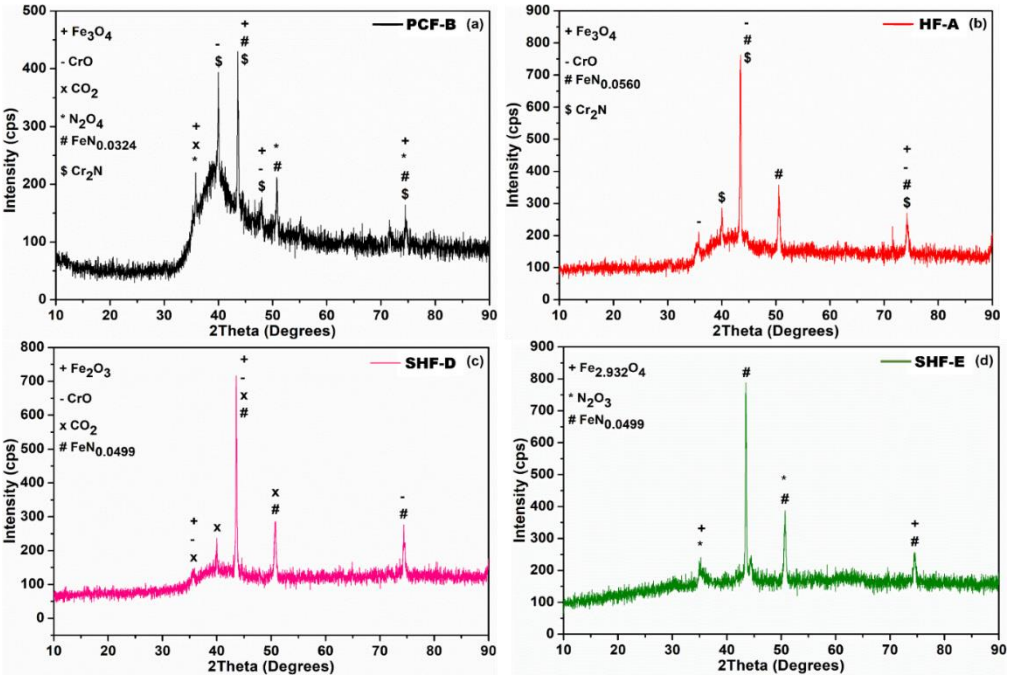

Figure 12. XRD analysis:**(a)** PCF-B, **(b)** HF-A, **(c)** SHF-D and **(d)** SHF-E.

The Figure13 shows the contrast in 'scaling' between MWS in ambient conditions (left) and inert Ar conditions (right) for SS316 turning chip sintered compacts. In ambient air, microwave-heated SS316 chips rapidly form a complex chromium–iron oxide layer, hindering atomic diffusion and raising the activation energy for neck formation. The resulting necks are brittle, discontinuous weakening foam integrity, yielding low SEA values for PCF, HF and SHF in air (22.08, 17.07, 23.87 J/g) [22]. Contrast this with the right side (Ar conditions), where the foam exhibits a relatively clean, metallic surface with minimal scaling. The sharp edges and complex geometries of the SS316 turning chips, as discussed, act as micro-antennas, concentrating microwave energy precisely at the contact points. This localized energy input, coupled with an unhindered metallic surface, allows for rapid and efficient solid-state diffusion, leading to the formation of well-defined metallic sintering necks. This is quantitatively confirmed by the improvement in SEA values under inert atmosphere MWS, with PCF showing ~22% increase (28.45 J/g), followed by ~12% increase in SHF (27.069 J/g) and ~30% increase for HF (24.60 J/g). Thus, the results highlight that controlling the MWS atmosphere is critical to achieving metallurgically bonded foams with superior structural integrity and energy absorption performance.

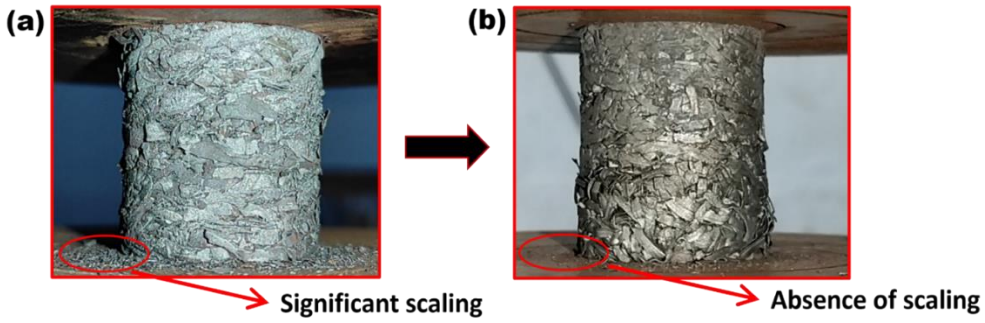

Figure 13. Compression testing of PCF sintered by microwave heating under **(a)** ambient atmosphere, showing surface scaling and **(b)** inert argon atmosphere, exhibiting minimal scaling.

4. Conclusion

The present study demonstrates that SS316 metal foams can be effectively fabricated from turning chips through solid-state microwave sintering, where metallurgical bonding between chip surfaces is established during the sintering stage. When processing in an Ar environment, the thermodynamic starting point of sintering is markedly altered. The unique geometry of the serrated turning chips, which act as micro-antennas, concentrates the microwave field at the sharp edges and contact points. This interaction creates 'geodesics' (effortless energy pathways) directly between the contact points of adjacent chips. Atoms are no longer climbing; they are guided along these energy-rich paths, accelerating the rate of surface diffusion. The outcome is not merely faster neck growth, but geometrically precise fusion dictated by the electromagnetic field, not by random thermal motion.

(1) A comparative assessment of three types of foams PCF, HF and SHF was carried out at microwave sintering temperatures of 1050 °C and 1200 °C in Ar atmosphere. PCF-B accounted for a highest SEA of 28.45 J/g with a porosity of 54.6 % and density of 3.58 g/cm^3. HF-D resulted in lower SEA of 23.81 J/g, associated with its reduced porosity (35.4 %) and higher density (5.1 g/cm^3). SHF-E achieved a high SEA of 27.069 J/g while maintaining high porosity (54.66%) and low density (3.54 g/cm^3), along with an extended plateau region, indicating stable and progressive energy absorption.

(2) The enhanced energy absorption behaviour of the foam is attributed to progressive deformation, including chip bending, flattening and buckling around inter-chip voids and larger pores (Figure 14). Sintering in Ar atmosphere improved the formation of well-defined sintering necks, facilitating strain propagation across the foam structure. This improvement can be attributed to the suppression of dense, adherent Fe_2O_3 layers, which typically develop under ambient atmosphere.

(3) Overall, the proposed metal foam fabrication route *i.e.* reusing of SS316 turning chips in solid state combined with green microwave sintering and low-cost, readily available space holder (urea) to generate tailored porosity demonstrates strong alignment with sustainable manufacturing principles such as SDG-12.

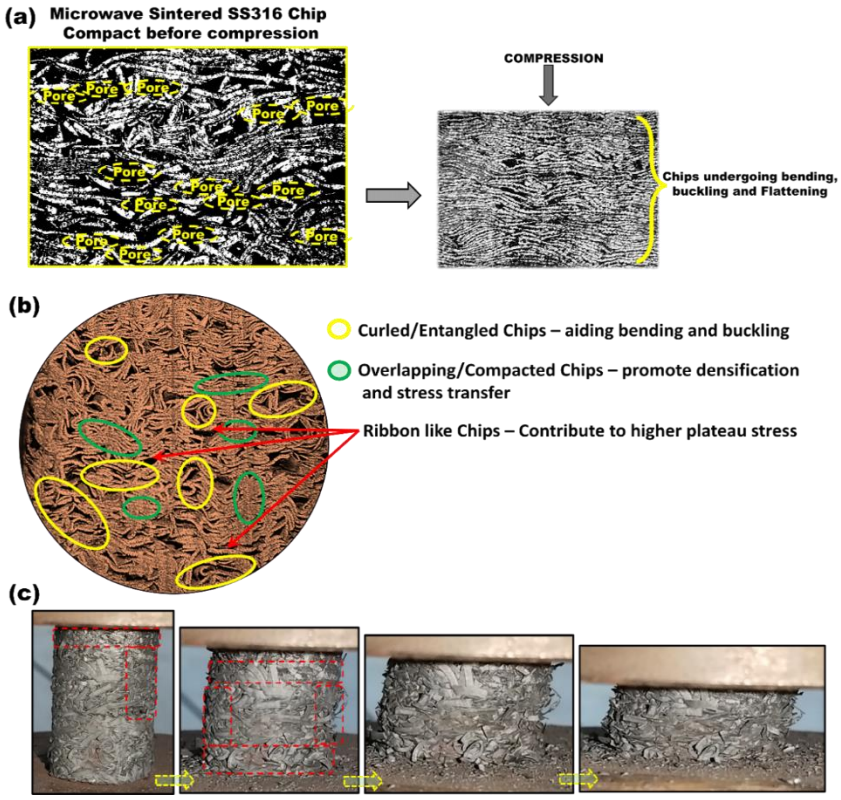

Figure 14. Illustrative schematic depicting **(a)** Progressive deformation of microwave-sintered SS316 chip foam; **(b)** key chip morphologies with their mechanical functions and **(c)** Deformation morphology of SS316 chip-based foam under compressive loading.

Data availability statement

The data or datasets that support the findings of this study are available from the corresponding author upon reasonable request.

Acknowledgements

The authors thank KLS Gogte Institute of Technology and Enerzi Microwave Systems Pvt. Ltd. for providing experimental and test facilities through Centre of Excellence on Industrial Microwave Heating Applications Development.

Authors' contribution

Sanket Shinde: investigation, visualization, data curation; Siddharama Adi: methodology, writing—original draft, formal analysis; Padmakumar Annasab Bajakke: methodology, visualization, validation; Vinayak Raghunath Malik: conceptualization, supervision, project administration, writing—review & editing. All authors have read and agreed to the published version of the manuscript.

Conflicts of interest

The authors declare that they have no known competing financial interests or personal relationships that could have appeared to influence the work reported in this paper.

References

[1] Edwin Basson. 2024 World Steel in Figures-world Steel Association. 2024. Available: https://worldsteel.org/data/world-steel-in-figures/world-steel-in-figures-2024/ (accessed on 15 October 2025).

[2] Murray JW, Jin X, Cleaver CJ, Azevedo JM, Liao Z, *et al*. A review of principles and options for the re-use of machining chips by solid, semi-solid or melt-based processing. *J. Mater. Process. Technol.* 2024, 331:118514.

[3] Global Industry Analysts, Inc Steel Scrap—Global Strategic Business Report. 2025. https://www.researchandmarkets.com/report/steel-scrap?srsltid=AfmBOoqBjm6Vdo_UYbGCACGEdgmN_gQX4fiej2wleGgTF70vGcNgSosT (accessed on 20 September 2025).

[4] Peng T, Wang Q. Application of regression analysis to optimize hot compaction processing in an indirect solid-state recycling of Mg alloy. In *Materials Science Forum*, Cairns, Australia, August 2–6, 2010, pp. 239–245.

[5] Dhiman S, Joshi RS, Singh S, Gill SS, Singh H, *et al*. A framework for effective and clean conversion of machining waste into metal powder feedstock for additive manufacturing. *Cleaner Eng. Technol.* 2021, 4:100151.

[6] Sofilić T, Rastovčan-Mioč A, Cerjan-Stefanović Š, Novosel-Radović V, Jenko M. Characterization of steel mill electric-arc furnace dust. *J. Hazard. Mater.* 2004, 109(1–3):59–70.

[7] Rane K, Nayak K, Date P, Tirumalai S. Solid state recycling of metal scrap for manufacturing net-shaped parts. *Int. J. Metallic Mater.* 2024, 1(1):21–38.

[8] Golvaskar M, Ojo SA, Kannan M. Recent advancements in material waste recycling: conventional, direct conversion, and additive manufacturing techniques. *Recycling* 2024, 9(3):43.

[9] Rao SR. *Resource Recovery and Recycling from Metallurgical Wastes*. Amsterdam: Elsevier, 2011.

[10] Tarıєва C. Technical characteristics of the recycling of iron-steel products. *Meas. Comput. Devices Technol. Processes* 2025, 1:377–382.

[11] United Nations, Department of Economic and Social Affairs, Sustainable Development. Available: https://sdgs.un.org/goals (accessed on 16 October 2025).

[12] Banhart J. Metal foams: production and stability. *Adv. Eng. Mater.* 2006, 8(9):781–794.

[13] Bajakke PA, Malik VR, Jambagi SC, Bhajantri V, Deshpande AS. Unidirectional flipped multiple-pass friction stir process: an innovative step in the fabrication of *in situ* Al–Cu composites. *Int. J. Adv. Manuf. Technol.* 2024, 134(3):1767–1787.

[14] Deng F, Liu Y, Lu X, Fan J. Improved stability of aluminum foam through heat treatment of foamable precursor. *Met. Mater. Int.* 2020, 26:1596–1601.

[15] Angelo PC, Subramanian R, Ravisankar B. *Powder Metallurgy: Science, Technology and Applications*, 2nd ed. Delhi: PHI Learning Pvt. Ltd, 2022.

[16] Malik VR, Bajakke PA, Jambagi SC, Bhajantri V, Deshpande AS. Comparative analysis of flipped and overlapped microwave sintered plus friction stir processed in-situ Al–Cu composites. *Emergent Mater.* 2024, 7:3091–3107.

[17] Hassan A, Alnaser IA. A review of different manufacturing methods of metallic foams. *ACS Omega* 2024, 9(6):6280–6295.

[18] Banhart J, Baumeister J, Weber M. Powder metallurgical technology for the production of metallic foams. In *Proceedings of the European Conference on Advanced PM Materials*, Birmingham, United Kingdom, October 23–25, 1995, p. 208.

[19] Kaya AC, Fleck C. Deformation behavior of open-cell stainless steel foams. *Mater. Sci. Eng., A* 2014, 615:447–456.

[20] Hu G, Xu G, Gao Q, Feng Z, Huang P, *et al*. Compressive properties and energy absorption behavior of 316L steel foam prepared by space holder technique. *Materials* 2023, 16(4):1419.

[21] Bekoz N, Oktay E. Effects of carbamide shape and content on processing and properties of steel foams. *J. Mater. Process. Technol.* 2012, 212(10):2109–2116.

[22] Shinde S, Bajakke PA, Malik VR. Sustainable fabrication of SS-316 foams from machining waste via microwave sintering: a new route for energy application properties. *Adv. Mater. Process. Technol.* 2025, pp. 1–14.

[23] Tsuda S, Kobashi M, Kanetake N. Producing technology of aluminum foam from machined chip waste. *Mater. Trans.* 2006, 47(9):2125–2130.

[24] Kanetake N, Tsuda S, Kobashi M. Foaming behavior of aluminum precursor produced from machined chip waste. In *Proceedings of the 5th International Conference on Porous Metals and Metallic Foams*, Montreal, Canada, September 5–7, 2007, p. 63.

[25] Haesche M, Lehmhus D, Weise J, Wichmann M, Mocellin ICM. Carbonates as foaming agent in chip-based aluminium foam precursor. *J. Mater. Sci. Technol.* 2010, *26*(9):845–850.

[26] Hangai Y, Kobayashi R, Suzuki R, Matsubara M, Yoshikawa N. Aluminum foam-filled steel tube fabricated from aluminum burrs of die-castings by friction stir back extrusion. *Metals* 2019, 9(2):124.

[27] Lela B, Jozić S, Krolo J, Dumanić I, Grgić K. Production of open cell foams out of aluminium chips. *Athens J. Technol. Eng.* 2021, 8(4):299–310.

[28] Krolo J, Lela B, Grgić K, Jozić S. Production of closed-cell foams out of aluminum chip waste: mathematical modeling and optimization. *Metals* 2022, 12(6):933.

[29] Grgić K, Lela B, Jozić S, Krolo J. Aluminium foams made of various aluminium alloys scrap and various foaming agents. In *11th International Conference Mechanical Technologies and Structural Materials (MTSM 2022)*, Split, Croatia, September 22–23, 2022, pp. 37–42.

[30] Suzuki R, Fujiwara K, Mita K, Hangai Y, Nishida S, *et al.* Fabrication of aluminum alloy foams from sheets using clad-chip extrusion technique. *Iran J. Sci. Technol. Trans. Mech. Eng*. 2025, 49(6):2547–2555.

[31] Soni H, Mashinini PM. An analysis on tool-chip interaction during dry machining of SS316 using textured carbide tools. *Arab J. Sci. Eng.* 2021, 46:7611–7621.

[32] Nagaraju KVV, Kumaran S, Rao TS. Densification kinetics of P/M austenitic (316L) stainless steels processed by rapid microwave hybrid heating method at various conditions. *Adv. Mater. Process. Technol.* 2021, 8(3):3539–3552.

[33] Bajakke PA, Malik VR, Jambagi SC, Deshpande AS. Corrosion behavior of novel AA1050/ZnO surface composite: a potential material for ship hull. *Mater. Lett.* 2020, 281:128602.

[34] Demirskyi D, Agrawal D, Ragulya A. A scaling law study of the initial stage of microwave sintering of iron spheres. *Scr. Mater.* 2012, 66(6):323–326.

[35] Zhu N, Hong Y, Qian F, Xu X. Kinetic model of urea-related deposit reactions. *Molecules* 2023, 28(5):2340.

[36] Schaber PM, Colson J, Higgins S, Thielen D, Anspach B, *et al*. Thermal decomposition (pyrolysis) of urea in an open reaction vessel. *Thermochim. Acta* 2004, 424(1,2):131–142.

[37] Zhong T, He K, Li H, Yang L. Mechanical properties of lightweight 316L stainless steel lattice structures fabricated by selective laser melting. *Mater. Des.* 2019, 181:108076.

[38] Wu Y, Lu X, Cho JIS, Rasha L, Whiteley M, *et al*. Multi-length scale characterization of compression on metal foam flow-field based fuel cells using X-ray computed tomography and neutron radiography. *Energy Convers. Manage.* 2021, 230:113785.

[39] Kader MA, Islam MA, Saadatfar M, Hazell PJ, Brown AD, *et al*. Macro and micro collapse mechanisms of closed-cell aluminium foams during quasi-static compression. *Mater. Des.* 2017, 118:11–21.

[40] Katona B, Orbulov IN. Structural damages in syntactic metal foams caused by monotone or cyclic compression. *Period. Polytech. Mech. Eng.* 2017, 61(2):146–152.

[41] Malik V, Sanjeev NK, Hebbar HS, Kailas SV. Finite element simulation of exit hole filling for friction stir spot welding—A modified technique to apply practically. *Procedia Eng.* 2014, 97:1265–1273.

[42] Chang L, Mukahiwa K, Volpe L, Scenini F. Effect of machining on oxide development in type 316L stainless steel in high-temperature hydrogenated water. *Corros. Sci.* 2021, 186:109444.

[43] Abdullah NAZ, Sani MSM, Salwani MS, Husain NA. A review on crashworthiness studies of crash box structure. *Thin-Walled Struct.* 2020, 153:106795.

[44] Reguera E, Díaz-Aguila C, Yee-Madeira H. On the changes and reactions in metal oxides under microwave irradiation. *J. Mater. Sci.* 2005, 40:5331–5334.

[45] Ali S, Abdul Rani AM, Ahmad Mufti R, Ahmed SW, Baig Z, *et al*. Optimization of sintering parameters of 316L stainless steel for in-situ nitrogen absorption and surface nitriding using response surface methodology. *Processes* 2020, 8(3):297.